chemosensors

MDPI

Article

Porous-Architecture-Driven Performance of Electrospun SnO_2 Nanofibers for Reliable H_2S Detection

Milica Počuča-Nešić [1,2,*], Katarina Vojisavljević [1], Slavica Savić Ružić [3], Zorica Marinković Stanojević [1,2], Aleksandar Malešević [1,2], Tian Tian [4], Nan Ma [4], Rong Qian [4], Mao Huang [4], Matejka Podlogar [5], Goran Branković [1,2] and Zorica Branković [1,2]

1 Institute for Multidisciplinary Research, National Institute of the Republic of Serbia, University of Belgrade, 11000 Belgrade, Serbia; kvojisavljevic@imsi.bg.ac.rs (K.V.); mzorica@imsi.bg.ac.rs (Z.M.S.); amalesevic@imsi.bg.ac.rs (A.M.); goran.brankovic@imsi.bg.ac.rs (G.B.); zorica.brankovic@imsi.bg.ac.rs (Z.B.)
2 Center of Excellence for Green Technologies, Institute for Multidisciplinary Research, National Institute of the Republic of Serbia, University of Belgrade, 11000 Belgrade, Serbia
3 Biosense Institute, Center for Sensing Technologies, University of Novi Sad, 21000 Novi Sad, Serbia; slavicas@biosense.rs
4 Shanghai Institute of Ceramics, Chinese Academy of Sciences (SICCAS), Shanghai 201899, China
5 Department for Nanostructured Materials, Jožef Stefan Institute, 1000 Ljubljana, Slovenia; matejka.podlogar@ijs.si
* Correspondence: milicaka@imsi.bg.ac.rs

Abstract

Pure SnO_2 nanofibers were synthesized via an electrospinning method and subsequently calcined at 550 °C to investigate the structure–property relationship governing H_2S gas sensing performance. X-Ray diffraction confirmed the formation of the crystalline rutile-type SnO_2. FE-SEM and TEM methods revealed a hierarchically porous morphology with fiber diameters ranging from 70 to 160 nm. BET measurements indicated a high specific surface area of 75 m^2/g, consistent with the observed porous architecture. Gas sensing measurements toward H_2S revealed a pronounced response value of 25 at 200 °C with the response time of 23 s, both superior to those recorded for acetone, ethanol, and hydrogen. The enhanced sensitivity and dynamic response are attributed to the large surface area and interconnected porous network of the nanofibers, which provide the abundant active sites and facilitate efficient gas diffusion.

Keywords: SnO_2; H_2S sensor; electrospinning; cross-sensitivity; porous nanofibers

1. Introduction

Hydrogen sulfide (H_2S) is a highly toxic, corrosive, and flammable gas encountered in industries such as oil and gas, wastewater treatment, and mining. Acute exposure to concentrations above 100 ppm can cause rapid loss of consciousness and death, while chronic exposure at lower levels leads to neurological and respiratory disorders. Regulatory agencies such as OSHA (Occupational Safety and Health Administration) and NIOSH (National Institute for Occupational Safety and Health) have set exposure limits of 10–20 ppm (ceiling), with an immediately dangerous to life or health (IDLH) value of 100 ppm [1]. In nature, H_2S occurs near volcanoes, sulfur springs, hydrothermal vents, and wetlands. It is also released from crude oil, natural gas, sewage systems, and industrial waste processing. Upon atmospheric release, H_2S oxidizes into SO_2, contributing to acid rain and subsequent soil and water pollution. The gas's strong odor reminiscent of rotten eggs is detectable at low concentrations, but olfactory fatigue renders it undetectable at higher levels, increasing

Check for updates

Received: 26 December 2025
Revised: 21 January 2026
Accepted: 27 January 2026
Published: 1 February 2026

Copyright: © 2026 by the authors. Licensee MDPI, Basel, Switzerland. This article is an open access article distributed under the terms and conditions of the Creative Commons Attribution (CC BY) license.

the risk of unnoticed exposure. Therefore, reliable H_2S detection using gas sensors is essential for industrial safety, environmental monitoring, and even medical diagnostics via breath analysis [2]. Reliable real-time detection of H_2S is essential for ensuring workers' safety, preventing environmental contamination, and enabling medical diagnostics. This urgency is underscored by industrial accidents, such as fatalities in sewage systems caused by sudden high-concentration exposure [3], as well as medical studies linking elevated H_2S levels in human breath to various diseases [2] and mechanistic research implicating H_2S in liver disease pathophysiology [4].

Current detection technologies, including optical sensors [5], electrochemical sensors based on nanomaterial-modified electrodes [6], and chemiresistive sensors utilizing conductive polymers and inorganic oxides [7] vary in sensitivity, selectivity, response time, and suitability for field deployment [8–12].

Chemiresistive sensors based on semiconducting metal oxides (SMOX), such as SnO_2, are particularly attractive due to their low cost, scalability, and high sensitivity. However, pure SnO_2 sensors often require high operating temperatures (>200 °C) and suffer from limited selectivity and humidity interference, motivating the development of advanced nanostructures and composite materials [10–13]. Nanostructuring and the creation of porous morphologies significantly enhance gas sensor performance by increasing the density of active sites, facilitating rapid gas diffusion, and enabling efficient charge transfer [11–16].

Various synthesis methods including hydrothermal [17–19], spray pyrolysis [2,20–22], sol-gel [23–25], electrospinning [11,26–32], flame synthesis [33], colloidal wet chemical synthesis [34], and green synthesis [35] have been employed to fabricate SnO_2 nanostructures for gas sensing applications. Recent studies have demonstrated that SnO_2 nanowires, nanotubes, and hollow fibers exhibit superior sensitivity and selectivity for H_2S detection compared to bulk or thin-film counterparts.

Among these, electrospinning stands out for its ability to produce continuous high-aspect-ratio nanofibers with tunable porosity and morphology, enabling scalable fabrication of sensor devices with enhanced surface area and gas accessibility [12,14,36]. Electrospinning as a simple, cost-effective, and versatile technique is widely used for synthesizing one-dimensional porous ceramic nanofibers. In this process, ultrafine fibers are produced by applying a high voltage, which causes a polymer solution or polymer melt to form a charged jet that elongates and solidifies into long continuous fibers. Various parameters influence the morphology of the resultant nanofibers, including the properties of the precursor solution (type of polymer, polymer and metal ion concentrations, and solvent properties) and experimental setup conditions (applied voltage, distance between the spinneret and collector, and feeding rate of precursor solution), as well as environmental factors such as temperature and humidity [37,38]. From this perspective, the changing of solution parameters can be used to tailor the nanofibers' structure and morphology. The polymer agent in ceramic precursor solutions is used to adjust the solution's viscosity, assist in jet formation, and to control the nanofibers' morphology [39]. On the other hand, Wali et al. reported on the preparation of various one-dimensional nanomorphologies of SnO_2 by controlling the tin concentration in the precursor solution [26].

Despite recent advances, the systematic control of porosity and morphology in electrospun SnO_2 nanofibers for optimized H_2S sensing remains underexplored. In this work, electrospinning parameters identified through preliminary experiments and guided by the established literature were applied to engineer nanofibers with enhanced surface area and controlled pore structure with the hypothesis that these features would lead to improved sensitivity, preferential response, and response times toward H_2S. The materials are characterized using SEM, TEM, XRD, and BET surface area analysis, and their H_2S

sensing performance is evaluated in terms of sensitivity, selectivity, response/recovery time, and stability. The results are compared with the recent literature to evaluate the practical relevance and potential applicability of the proposed approach.

2. Materials and Methods

2.1. Materials

High-purity reagent-grade chemicals were carefully selected for the electrospinning synthesis of SnO_2 nanofibers. These included tin(II) chloride dihydrate ($SnCl_2 \cdot 2H_2O$, purity $\geq$ 98%, Acros Organics, Geel, Belgium), polyvinylpyrrolidone ($(C_6H_9NO)_n$, PVP, M_w ~1,300,000, Sigma-Aldrich Chemie GmbH, Steinheim am Albuch, Germany), absolute ethanol (C_2H_5OH, purity $\geq$ 99.8%, Honeywell, Seelze, Lower Saxony, Germany), and N,N-dimethylformamide ($HCON(CH_3)_2$, DMF, purity $\geq$ 99.9%, Sigma-Aldrich, St. Louis, MO, USA). Additionally, the organic functional additive α-terpineol ($C_{10}H_{18}O$, Aldrich, St. Louis, MO, USA) played a crucial role in the thick film fabrication process, enhancing the structural and functional integrity of the sensor.

2.2. Synthesis of Multichannel SnO_2 Nanofibers

One-dimensional hollow SnO_2 nanofibers with multichannel structure were prepared via a single-nozzle electrospinning technique.

Initially, the solution parameters were selected based on previously published studies [12,26,40] and theoretical considerations [37,38] with the aim of obtaining a precursor solution suitable for stable electrospinning of SnO_2 nanofibers. In the preliminary stage, PVP concentrations of 6, 6.5, and 7 wt.% were investigated together with tin-to-PVP mass ratios of 1:2, 1:2.5, and 1:3. An equal volume ratio of ethanol and DMF was used as the initial solvent composition. Among these conditions, the combination of 7 wt.% PVP and a tin-to-PVP ratio of 1:2.5 resulted in the most favorable fiber formation.

To obtain continuous and homogeneous nanofiber mats, the solvent composition was subsequently adjusted by increasing the ethanol content, leading to a final DMF:EtOH volume ratio of 2:3. This solvent ratio was selected because it improved fiber thickness, uniformity, and deposition yield.

To synthesize the electrospinning precursor solution, 0.9032 g of PVP was dissolved in 9.2 mL of solvent mixture composed of DMF and EtOH (v/v 2:3). The solution was magnetically stirred at 700 rpm for 2.5 h at room temperature. Separately, 0.3454 g of $SnCl_2 \cdot 2H_2O$ was dissolved in 5 mL of the same solvent mixture and preheated at 45 °C in an oil bath while stirring for 15 min. The PVP solution was then gradually added to the Sn precursor solution, and the resulting mixture was homogenized by stirring at 700 rpm for 2 h at 45 °C, followed by stirring overnight at room temperature.

Once a stable precursor solution was achieved and bead-free, continuous nanofibers were reproducibly deposited on alumina substrates, the electrospinning parameters—namely applied voltage, solution flow rate, tip-to-collector distance, and collector rotational speed—were further fine-tuned to improve fiber uniformity, mat homogeneity, and deposition efficiency. The tested parameter ranges and the final selected values are summarized in the Table 1.

The prepared electrospinning solution was loaded into a 10 mL syringe equipped with a 21-gauge stainless steel needle (inner diameter: 0.51 mm) and deposited onto aluminum foil for 40 min. Electrospinning was carried out at a flow rate of 0.7 mL/h under an applied voltage of 20 kV with a tip-to-collector distance of 18 cm and a collector rotational speed of 1000 rpm. The process was performed under controlled environmental conditions of 22–24 °C and 35–40% relative humidity (RH).

Table 1. Tested ranges and final selected electrospinning parameters for the fabrication of SnO_2 nanofibers.

Parameter	Tested Range	Final Value
voltage [kV]	19–22	20
tip-to-collector distance [cm]	15–20	18
solution flow rate [mL/h]	0.5–1	0.7
collector rotational speed [rpm]	900–1200	1000

The as-spun fibers were subsequently thermally treated in air using a four-step calcination process with a heating rate of 1 °C/min. The fibers were held at 200 °C and 250 °C for 30 min each, followed by 347 °C for 1 h and, finally, 550 °C for 1 h, yielding crystalline SnO_2 nanofibers (see Figure S1).

2.3. Characterization Methods

The morphological characteristics of the synthesized SnO_2 fibers were analyzed using a field emission scanning electron microscope (FE-SEM (SEM, Verios 4G HP, Thermo Fisher Scientific Inc., Waltham, MA, USA) and a conventional 200 kV transmission electron microscope (TEM, JEOL JSM-2100, Jeol Ltd., Tokyo, Japan). Prior to FE-SEM analysis, the powder was spread onto a carbon tape and sputter-coated with a thin layer of gold to minimize charging during imaging. Images were acquired in secondary electron mode at 5 kV (2 kV). For TEM analysis, the sample was ultrasonically dispersed in absolute ethanol for 10 min, and a drop of the suspension was deposited onto a carbon-coated Ni TEM grid prior to observation.

The XRD patterns of the samples were collected using a Rigaku SmartLab diffractometer and Cu $K\alpha$ and K_β radiation. The XRD data were collected in a 2θ range between 20 and 90° with a step size of 0.02° and a counting rate of 3°/min. Both the lattice parameter and the crystallite size, D_{xrd}, values were obtained by fitting the data collected in the space group $P4_2/mnm$ (No.136) using the integrated PDXL 2 software (Rigaku Co., Ltd., Tokyo, Japan). D_{xrd} values were extracted by applying the Halder–Wagner (HW) method.

Nitrogen adsorption–desorption isotherms were measured at −196 °C using an ASAP 2020 surface area and porosity analyzer (Micromeritics, Norcross, GA, USA). Prior to analysis, the sample was degassed under vacuum at 120 °C for 6 h to remove moisture and physisorbed species. The specific surface area (S_{BET}) was calculated using the Brunauer–Emmett–Teller (BET) equation applied to the linear region of the adsorption isotherm in the relative pressure range P/P_0 = 0.05–0.30. The mesopore volume (V_{meso}) and mesopore size distribution, including the average mesopore diameter ($\underline{d}_{meso}^{\mathrm{BET}}$), were obtained from the desorption branch of the isotherm using the Barrett–Joyner–Halenda (BJH) method. Using the obtained S_{BET} values for SnO_2 NFs and the formula for the BET equivalent particle diameter, $L_{\mathrm{BET}} = (\Psi_A \cdot \Psi_v^{-1})/(S_{\mathrm{BET}} \cdot \rho_t)$, the primary particle size value was calculated. In this equation, $(\Psi_A \cdot \Psi_v^{-1})$ is the shape factor ratio (=6), S_{BET} is the specific surface area of the SnO_2 NFs, and ρ_t is the theoretical density of SnO_2 (6.95 g/cm^3) [41].

2.4. Fabrication and Testing of SnO_2 Gas Sensors

The SnO_2 NF sensor was prepared using the screen printing technique. The powder was mixed with a small amount of α-terpineol to form uniform slurry, which was subsequently printed onto a 4 mm × 4 mm Al_2O_3 substrate. The substrate featured a pair of gold interdigitated electrodes on the front side for resistance measurements and a platinum microheater on the reverse side for temperature control. The printed thick film was then

heat-treated at 160 °C for 1 h to remove the organic binder and improve adhesion between the sensing layer and the substrate.

The gas sensor was tested using a custom-built dynamic testing system. The gas sensing measurements were conducted using the following setup: mass flow controllers (MFC, S48 300/HMT, HORIBA Precision Instruments, Beijing, China), a test chamber with a volume of approximately 26 cm^3, calibrated H_2S gas (10 ppm H_2S in air, Shanghai Wetry Standard Gas Analysis Technology Co., Ltd., Shanghai, China), and synthetic air (99.999%, Shanghai Laokang Chemistry Technology, Shanghai, China). A schematic diagram of the experimental setup can be found in the [42]. The target gas concentration was precisely controlled by mass flow controllers, and the total gas flow was set to 100 mL/min. The sensing properties were investigated by recording the change in resistance by a source electrometer Keithley DAQ6510 (Solon, OH, USA) in the presence of analyte gases and different temperatures controlled by a dc power supply system (RIGOL DP832). Four sensors were inserted in a four-channel multiplexer and measurements were executed from room temperature up to 400 °C depending on the type of the analyte gas. To determine the performance of the sensors, gas sensing tests were carried out three and in some cases five times at a constant temperature. At each working temperature, synthetic air and analyte gases (10 ppm H_2S, acetone, and ethanol, as well as 50 ppm H_2) were sequentially introduced into the gas sensing chamber. Each cycle consisted of 10 min of synthetic air followed by 10 min of analyte gas. To evaluate the sensor response at different concentrations of the target analyte, H_2S was introduced at 0.5, 1, 2, 5, and 10 ppm under the previously determined optimal operating temperature. The sensor response was calculated as $S = R_a/R_g$, where R_a and R_g denote the sensor resistance in the presence of the synthetic air and target gas, respectively.

The response time was defined as the time required for the sensor to reach 90% of its maximum signal upon exposure to H_2S, while the recovery time was defined as the time needed for the signal to return to 10% above the baseline after removal of the gas.

The cross-sensitivity of the SnO_2 NF sensor was evaluated by exposing the sensing layer to different gases, including ethanol, acetone, and hydrogen, in separate experiments under the respective optimal measurement temperatures at which these gases exhibit the highest response. The concentrations of these gases were equal to or higher than that of H_2S.

3. Results and Discussion

The crystalline structure and phase composition of calcined nanofibers were characterized by XRD analysis. The diffraction peaks observed in the pattern (Figure 1), corresponding to the (100), (101), (200), (211), and (220) planes, confirm the formation of cassiterite SnO_2 with a rutile-type tetragonal unit cell (S.G. P42/*mnm*, JCPDF 41-1445). The calculated lattice parameters a = b = 4.7365 Å and c = 3.1890 Å are consistent with values reported in the literature. The crystallite size D_{xrd}, estimated from the XRD data, is approximately 5 nm.

The micrographs presented in Figure 2 reveal the microstructure of electrospun fibers before and after calcination. The electrospinning process produced randomly distributed SnO_2/PVP nanofibers with smooth surfaces and uniform diameters along their length (Figure 2a). After calcination, the fibers retained this continuous fibrous morphology, though their diameters decreased as a result of PVP decomposition and shrinkage during thermal treatment (Figure 2b).

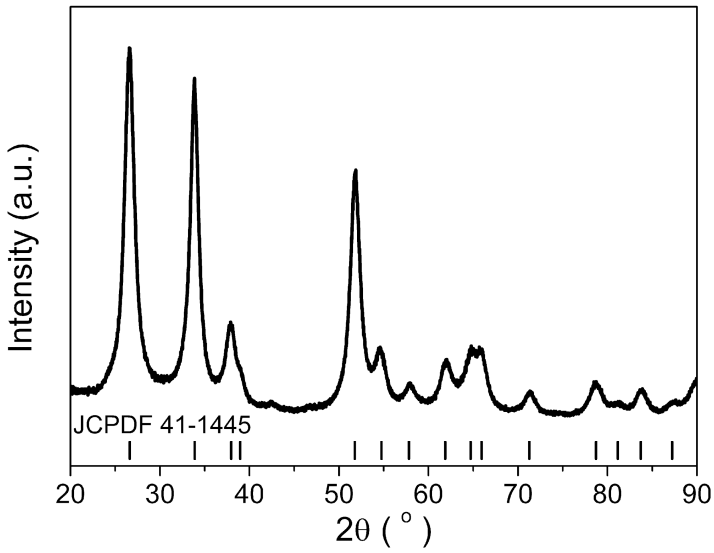

Figure 1. XRD pattern of calcined SnO_2 nanofibers.

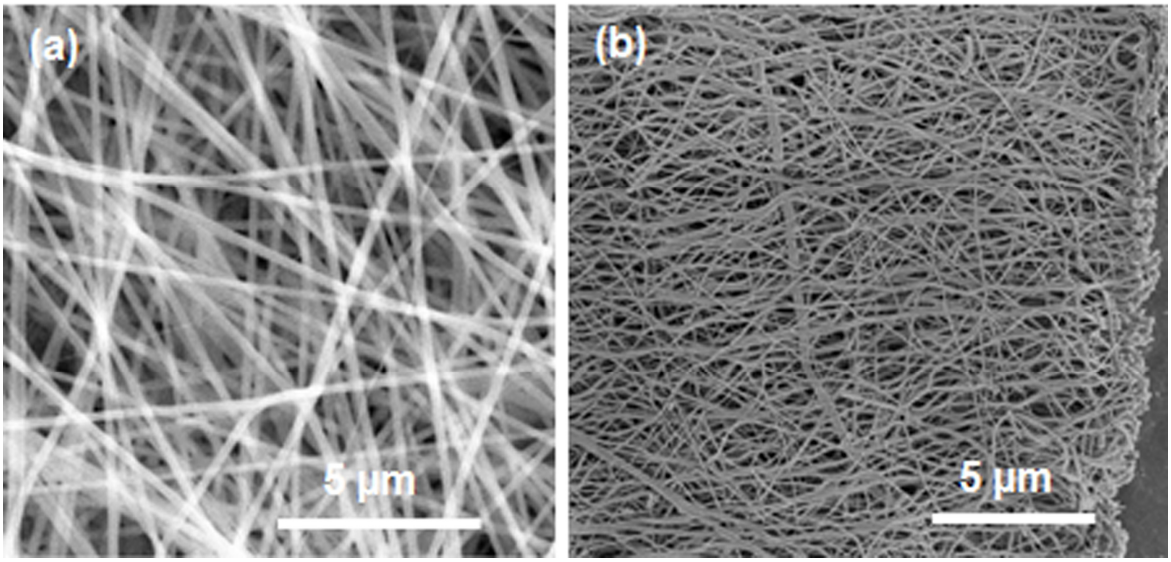

Figure 2. SEM micrographs of (**a**) SnO_2/PVP fibers and (**b**) calcined SnO_2 nanofibers.

Calcination significantly influences the morphology of as-spun SnO_2 nanofibers. During PVP decomposition, the release of CO_2 and H_2O promotes fiber expansion, thereby enhancing porosity and surface area [29,43]. Variations in heating rate further tune the structural characteristics, enabling the formation of hollow, porous, or dense fibers [44,45]. However, excessively high heating rates may lead to structural collapse and the formation of shortened fibers [29]. As shown in Figure 3a, a low heating rate of 1 °C/min produced NFs with rough surfaces, attributed to the gradual decomposition of PVP. Although lower heating rates are often reported to yield dense nanofibers [29,44], the obtained SnO_2 NFs are distinctly multiporous with internal channels evident (Figure 3b).

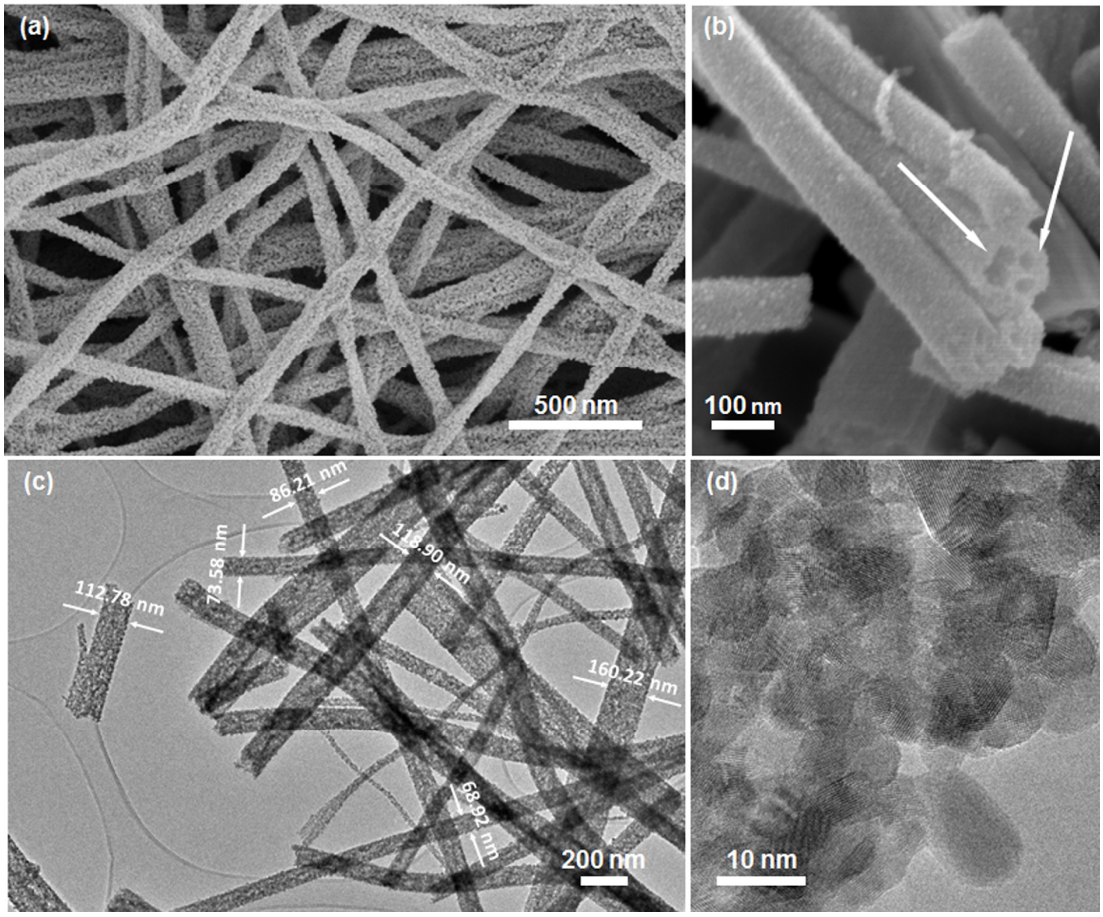

Figure 3. FE-SEM micrographs: (**a**) SnO_2 nanofibers calcined at 550 °C (low magnification) and (**b**) nanofibers with multi-channels (high magnification, marked with arrows). TEM micrographs: (**c**) nanofibers' diameter and (**d**) particle size.

The fiber diameters range from 70 to 160 nm (Figure 3c). This observation aligns with the findings of Wali et al., who demonstrated that multiporous SnO_2 nanofibers can be achieved by adjusting the tin concentration in the precursor solution and applying a slow heating rate during calcination [26]. High-resolution TEM images further reveal that the NFs consist of interconnected nanoparticles with uniform morphology and an average particle size below 10 nm (Figure 3d).

The specific surface area, a morphology-dependent property, plays a crucial role in determining the sensing performance of materials. For the SnO_2 NFs, nitrogen adsorption–desorption isotherms were measured and analyzed using the Brunauer–Emmett–Teller (BET) method. According to IUPAC classification [46], the obtained isotherms (Figure 4a) correspond to type IV, which is characteristic of mesoporous materials. The calcined SnO_2 NFs exhibited a specific surface area of 75 m^2/g. The pore size distribution (Figure 4b), calculated using the Barrett–Joyner–Halenda (BJH) method from the desorption branch of the isotherm, revealed an average pore diameter of 4.5 nm. The primary particle size, calculated to be 11.5 nm, is consistent with TEM observations.

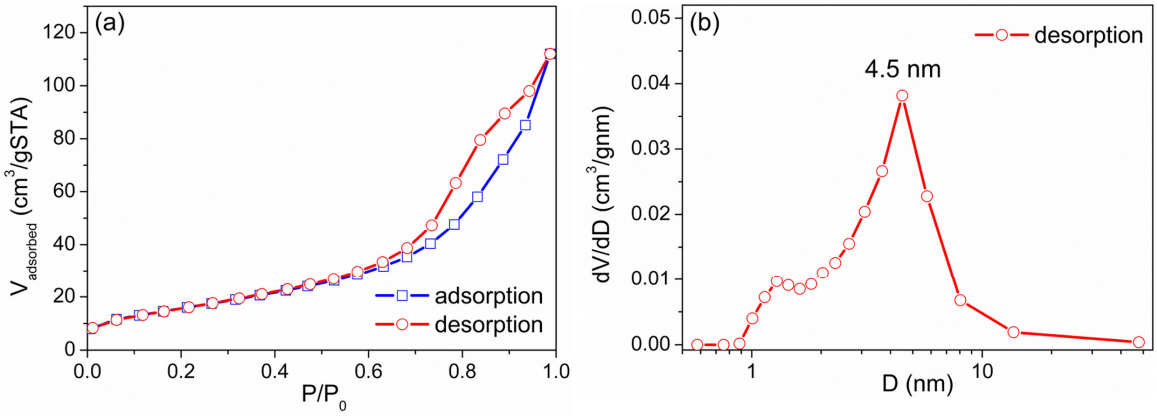

Figure 4. (**a**) Nitrogen adsorption–desorption isotherm and (**b**) pore size distribution plot of SnO_2 NFs.

Mesoporous materials with high specific surface areas are excellent candidates for gas sensing applications, as they offer numerous active sites for adsorption and promote enhanced interaction between gas molecules and the sensing layer. Figure 5a,b show the surface of the thick film prepared from calcined SnO_2 NFs. These micrographs reveal a highly porous fibrous structure that is preserved during film formation. The individual fibers form a continuous network, providing pathways for gas diffusion and efficient exposure of active sites for gas–solid reactions.

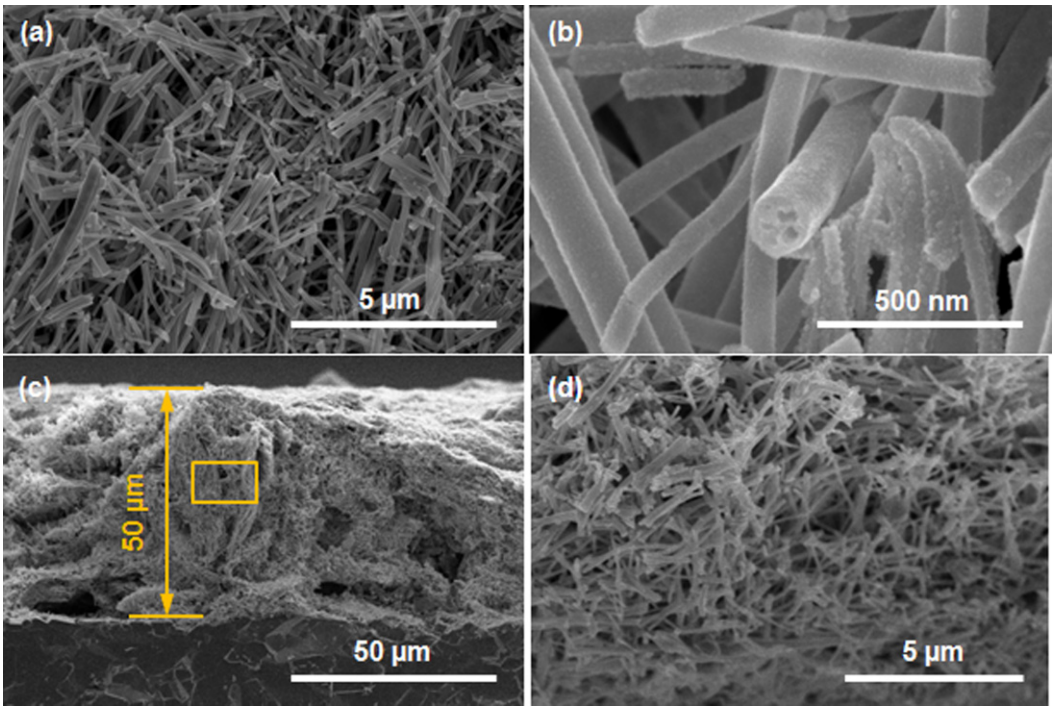

Figure 5. SE Micrographs of surface (**a**,**b**) and cross-section (**c**,**d**) of SnO_2-NF-based thick film, where (**d**) represents a higher-magnification view of the rectangular region highlighted in (**c**).

The cross-sectional morphology reveals that the film has a thickness of approximately 50 µm, confirming that the porous structure extends throughout the entire volume and showing no evidence of the collapse of the fibrous network (Figure 5c,d).

The gas sensing behavior of n-type MOX sensors is governed by the adsorption and desorption of gaseous species on the sensors' surface. In ambient air, oxygen molecules are adsorbed on the SnO_2 surface and extract electrons from the conduction band, forming

ionized chemisorbed oxygen species (O_2^-, O^-, O^{2-}) depending on the operating temperature, which leads to the formation of an electron depletion layer at the grain surface. At relatively low temperatures, O_2^- species dominate, whereas O^- becomes the predominant form at typical operating temperatures of SnO_2-based sensors (150–400 °C), while O^{2-} may appear at higher temperatures. Upon exposure to a reducing gas such as H_2S, the gas reacts with these chemisorbed oxygen species, releasing trapped electrons back into the conduction band and resulting in a decrease in the electrical resistance of the sensing material [7,47–49]. The extent and kinetics of these surface reactions are strongly influenced by the operating temperature, which affects both oxygen ionization processes and charge carrier mobility. Given that the optimal operating temperature of a SnO_2-NF-based sensor is 200 °C, we could assume that the chemisorbed oxygen species on the SnO_2 surface are generally dominated by O^- ions, which are primarily responsible for surface redox reactions with reducing gases. Accordingly, the possible surface reactions can be expressed as follows [7].

$$2H_2S_{(g)} + 3O^-_{2\,(ads)} \rightarrow 2H_2O_{(g)} + 2SO_{2(g)} + 3e^- \quad (1)$$

$$H_2S_{(g)} + 3O^-{}_{(ads)} \rightarrow H_2O_{(g)} + SO_{2(g)} + 3e^- \quad (2)$$

To determine the optimum operating temperature, the sensing responses of prepared SnO_2-NF-based sensors were evaluated in the (25–250) °C range under exposure to 10 ppm of H_2S (Figure 6a).

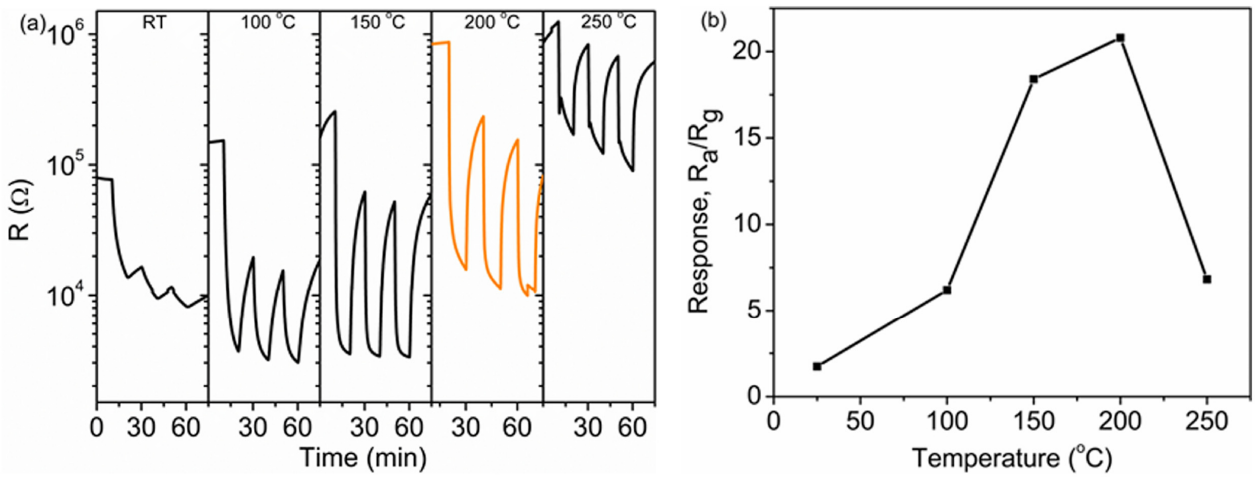

Figure 6. (**a**) Resistance curves of SnO_2-NF-based sensors at different temperatures toward 10 ppm H_2S and (**b**) sensor responses to 10 ppm H_2S as a function of operating temperature.

The response increased with temperature up to 200 °C, indicating that lower temperatures do not provide sufficient energy to activate oxidation processes and reaction with H_2S (Figure 6b). At this temperature, the surface reaction between adsorbed oxygen species and gas molecules is enhanced, yielding the maximum sensor response. Further increase in temperature resulted in a significant decrease in response, likely due to reduced gas adsorption, and the possible desorption of oxygen species, which increases the number of electrons in the conduction band and thereby raises the material's resistance. Consequently, 200 °C was selected as the optimum operating temperature for subsequent measurements. At this temperature, the sensors' response reached 20.8, which is comparable to values reported in the literature for both pure [20,48] and SnO_2-based sensors [27,50–53]. The enhanced sensitivity and faster kinetics of our SnO_2 NFs can be attributed to their high surface area and hierarchically porous network, which provide abundant active sites and facilitate gas diffusion.

Table 2 presents a comparative overview of SnO_2-based sensors for H_2S detection, including synthesis methods, operating temperatures, and response times, with our results included for reference. As shown, most reported sensors operate at temperatures of 200 °C or higher, which aligns with the optimum temperature identified in our study. However, our work also demonstrates that high sensitivity can be achieved at 150 °C, accompanied by more stable response behavior (Figure 6).

To assess the short-term repeatability of the gas sensing performance, the sensor was exposed to 10 ppm H_2S at 200 °C over four successive cycles. The corresponding dynamic response is presented in Figure 7.

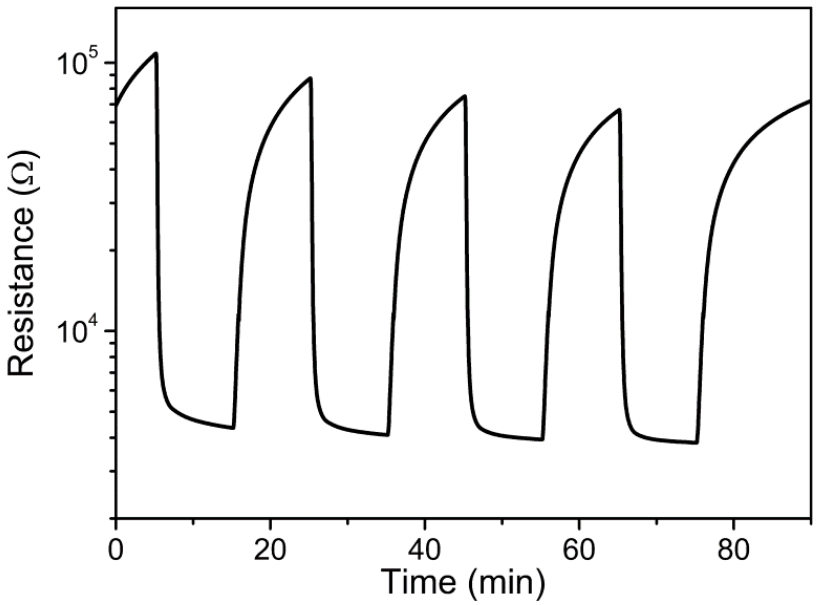

Figure 7. The sensors' response to four repeated exposures to 10 ppm H_2S at 200 °C.

The obvious decrease in sensor response upon successive exposure to 10 ppm H_2S can be attributed to the partial retention of gas molecules, either H_2S or reaction products on the sensor's surface. These species, due to their slow desorption, can temporarily occupy active adsorption sites. Additionally, the strong affinity of SnO_2 for H_2S leads to the formation of tin sulfide (SnS_x) phases that are difficult to reoxidize once formed [54], along with the formation of sulfite and sulfate species in SnO_2-based sensors [55]. These reactions occur simultaneously with those given by Equations (1) and (2) and, consequently, decrease the sensors' response. However, the high specific surface area and large number of accessible sites mitigate this effect, facilitating gas diffusion through the porous nanofiber network and across the film volume. As a result, the sensor response highlights the benefit of the synthesis method in generating a porous microstructure that improves surface accessibility and overall performance. At the same time, it also indicates that problems related to surface poisoning can be mitigated by surface modifications with suitable additives or by specific technical procedures such as cleaning the sensors' surface using the quick and short heating of the sensor at 500 °C [55,56].

Table 2. Comparative study of SnO_2-based sensors for H_2S detection, including synthesis methods, operating temperatures, and response times.

Material	Form	Synthesis Method	H_2S Concentration [ppm]	Operating Temperature [°C]	Sensor Response [1] [/] or [%]	t_{res} [s]	Ref.
SnO_2	nanofibers	electrospinning	1	200	5.44	91	this work
SnO_2	nanofibers	electrospinning	5	200	12.41	44	this work
SnO_2	nanofibers	electrospinning	10	200	24.29	23	this work
SnO_2	-	electrospinning	10	200	19.83%	≈90	[27]
SnO_2	nanofibers	electrospinning	50	250	10.49	≈70	[50]
SnO_2	dense nanofibers	electrospinning	5	300	2.6	≈40	[55]
SnO_2	nanotubes	electrospinning	5	300	4.7	≈70	[55]
SnO_2	hollow nanofibers	electrospinning	100	300	118.6	30	[12]
SnO_2	full nanofibers	electrospinning	100	300	45.8	60	[12]
SnO_2	-	co-precipitation	10	275	1.06	-	[52]
Fe-SnO_2	-	co-precipitation	10	275	3.1	-	[52]

[1] Sensor response $S = R_a/R_g$ [/]; $S = [(R_a - R_g)/R_g] \times 100$ [%].

The dynamic response of the SnO_2 NF sensor to varying H_2S concentrations was investigated at the optimum operating temperature of 200 °C. As presented in Figure 8, increasing the H_2S concentration from 0.5– to 10 ppm led to a rise in response values from 3.4 to 15.2. This upward trend indicates that a higher concentration of H_2S molecules enhances the surface reaction with adsorbed oxygen species, resulting in a greater change in sensor resistance. The response times for 0.5, 1.0, 2.0, 5.0, and 10 ppm H_2S were 156 s, 91 s, 67 s, 44 s, and 33 s, respectively. The observed decrease in response time with increasing gas concentration can be attributed to the greater number of gas molecules available for surface reactions.

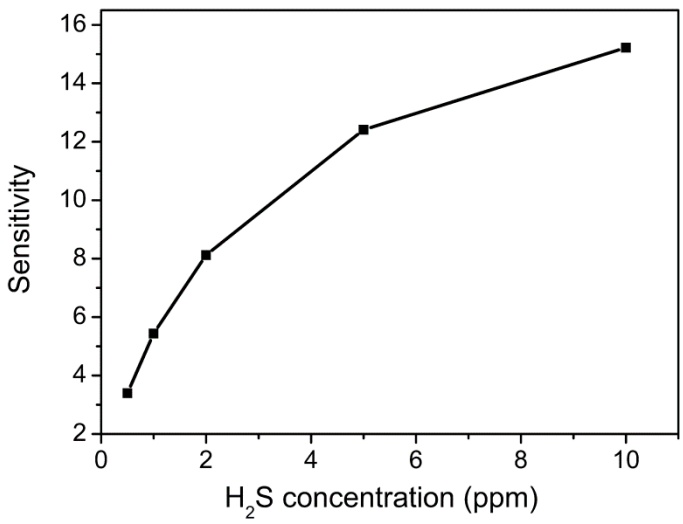

Figure 8. Sensitivity dependence of SnO_2-NF-based sensor toward H_2S concentrations in the range of 0.5–10 ppm.

At lower concentrations, the diffusion of H_2S molecules through the porous network of SnO_2 NFs becomes a rate limiting factor, thereby prolonging the response time. At higher concentrations, the reaction rate between H_2S and the chemisorbed oxygen species is enhanced. The increased probability of interaction accelerates electron transfer, reduces

resistivity more rapidly, and allows the sensor to reach equilibrium in a shorter time. However, after each exposure cycle, the baseline resistance did not fully return to its initial value. This behavior is consistent with the gradual decrease in sensor response observed during repeated exposures to 10 ppm H_2S. The incomplete recovery suggests that a fraction of the adsorbed H_2S, or its reaction products, remained on the sensor surface, hindering complete desorption. Consequently, reliable recovery times could not be determined. Prolonged recovery, which is common in SnO_2-based H_2S sensors, can be attributed to the strong affinity of SnO_2 for H_2S, leading to the formation of tin sulfide (SnS_x) phases that are difficult to reoxidize once formed [54]. Additionally, the formation of sulfite and sulfate species in SnO_2-based sensors may further extend the recovery period [55].

The cross-sensitivity of the SnO_2-nanofiber-based sensors was evaluated by exposing them, in separate experiments, to possible interfering gases under their respective optimal conditions: acetone and ethanol (10 ppm, 300 °C) and hydrogen (50 ppm, 350 °C). These test conditions involved higher temperatures and, in the case of hydrogen, a higher concentration than those used for H_2S detection. As shown in Figure 9, the sensor exhibited a markedly higher response to H_2S compared with the other tested gases. Cross-sensitivity demonstrates that the sensor's response to possible interfering gases is negligible (ten times lower to acetone and ethanol) compared to its response to the target gas. This behavior can be attributed to the higher chemical affinity and stronger reducing nature of H_2S, whose reaction with adsorbed oxygen species proceeds more rapidly and releases a greater number of electrons into the SnO_2 conduction band. These results demonstrate that sensors based on mesoporous SnO_2 NFs exhibit strong cross-sensitivity toward H_2S and show potential for reliable detection in complex gas environments.

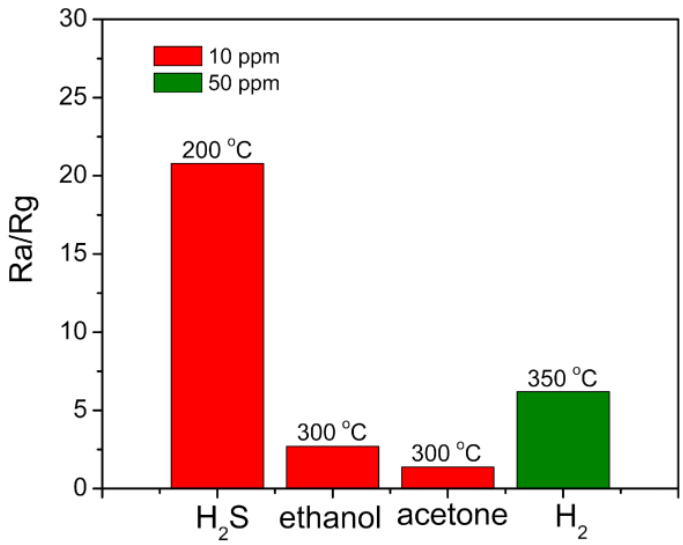

Figure 9. Comparison of gas sensing responses of SnO_2-nanofiber-based sensors to H_2S, ethanol, acetone, and H_2.

Additionally, the long-term stability of the sensor was assessed over a one-week period (Figure 10). Under repeated exposure to 10 ppm H_2S at 200 °C, the sensor maintained consistent sensitivity values with only minor fluctuations, confirming reliable operational stability.

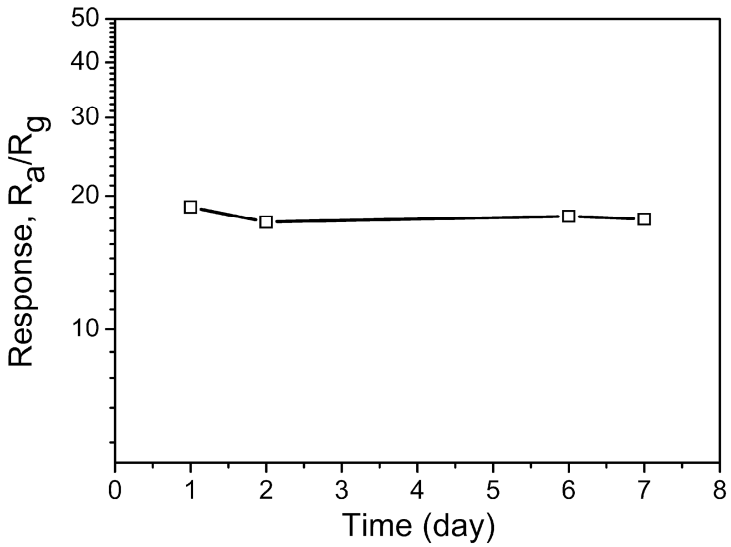

Figure 10. Long-term stability test of SnO_2-NF-based sensor toward 10 ppm H_2S at 200 °C.

4. Conclusions

Multiporous SnO_2 nanofibers with hierarchically porous architecture and high specific surface area were synthesized via electrospinning followed by controlled calcination. Structural and morphological analyses confirmed cassiterite-phase SnO_2 composed of interconnected nanoparticles (<10 nm) forming mesopores (~4.5 nm), while multichannel fibers (diameter 70–160 nm) contributed macroporous voids, yielding a surface area of 75 m^2/g with mesopores averaging 4.5 nm. Thick-film sensors fabricated from these nanofibers exhibited excellent sensitivity toward 10 ppm H_2S at 200 °C, with a maximum response of 24.29 enabled by the large surface area and open porous network that provide abundant active sites and facilitate rapid electron transfer.

Dynamic response measurements demonstrated reproducible performance across repeated cycles, while concentration-dependent studies revealed accelerated response times with increasing H_2S levels, underscoring efficient gas diffusion and reaction kinetics. Recovery was not fully complete, reflecting the strong interaction between H_2S and the SnO_2 surface; however, this highlights an important direction for future optimization aimed at improving long-term stability. Cross-sensitivity tests further confirmed a markedly stronger response to H_2S compared with acetone, ethanol, and hydrogen, emphasizing both the chemical affinity of H_2S and the robustness of the nanofiber design.

Overall, these results establish mesoporous SnO_2 nanofibers prepared via electrospinning as a reliable platform for toxic gas detection, combining high sensitivity, reproducibility, and selectivity. The synthesis route offers a versatile basis for engineering advanced porous nanostructures, and future work may explore doping, heterostructure formation, or flexible substrates to enhance recovery and broaden application in environmental monitoring and industrial safety.

Supplementary Materials: The following supporting information can be downloaded at: https://www.mdpi.com/article/10.3390/chemosensors14020032/s1, Figure S1: TG curve of the electrospun SnO_2 precursor nanofibers.

Author Contributions: Conceptualization, M.P.-N., K.V., S.S.R., G.B. and Z.B.; methodology, G.B.; Z.B., K.V., S.S.R. and N.M.; validation, K.V., S.S.R., N.M. and G.B.; formal analysis, M.P.-N., K.V., S.S.R., Z.M.S., T.T., N.M., R.Q. and M.H.; investigation, M.P.-N., K.V., S.S.R., Z.M.S., A.M., T.T., N.M., R.Q. and M.P.; resources, Z.B., N.M. and M.P.; data curation, K.V., N.M. and Z.B.; writing—original draft preparation, M.P.-N.; K.V. and S.S.R.; writing—review and editing, M.P.-N., S.S.R., K.V. and

Z.B.; visualization, K.V.; supervision, Z.B.; project administration, Z.B.; funding acquisition, Z.B. All authors have read and agreed to the published version of the manuscript.

Funding: This research was supported by the Science Fund of the Republic of Serbia, #GRANT No 7069, A new approach for multiple gas sensing with high sensitivity and selectivity—MULTISENSE; the Serbian Ministry of Science, Technological Development and Innovation (contract numbers: 451-03-136/2025-03/200053 and 451-03-136/2025-03/200358); Serbian Ministry of Education, Science and Technological Development and German Academic Exchange Service (DAAD) through Serbian–German bilateral project "Nanostructured semiconducting metal-oxides as gas sensors for medical diagnostics by breath analysis" (2020/2021) and Serbian Ministry of Science, Technological Development and the Ministry of Science and Technology of the People's Republic of China through Mobility Project "The cooperative study of high-performance and low-cost gas sensors for smart agriculture". The work of the Chinese team was funded through Scientific and technological cooperation projects between the Republic of Serbia and the People's Republic of China, the International Partnership Program of Chinese Academy of Sciences (No. 030GJHZ2022039FN and No. 030GJHZ2024069FN). The financial support of the Slovenian Research and Innovation Agency (ARIS) is gratefully acknowledged (Project No. J2-3051 and Program No. P2-0084).

Institutional Review Board Statement: Not applicable.

Informed Consent Statement: Not applicable.

Data Availability Statement: The original contributions presented in this study are included in the article/Supplementary Material. Further inquiries can be directed to the corresponding author.

Acknowledgments: We acknowledge the CEMM and JSI for the use of SEM and TEM.

Conflicts of Interest: The authors declare no conflicts of interest.

References

1. Occupational Safety and Health Administration (OSHA). Hydrogen Sulfide Hazards. U.S. Department of Labor. Available online: https://www.osha.gov/hydrogen-sulfide/hazards (accessed on 26 January 2026).
2. Liewhiran, C.; Punginsang, M.; Inyawilert, K.; Siriwalai, M.; Wisitsoraat, A. Selectivity toward H2S against various gaseous disease markers in exhaled breath of flame-produced CuO_x-loaded SnO_2 nanosensors. *Sens. Actuators B Chem.* **2025**, *424*, 136856. [CrossRef]
3. Song, H.; Wan, R.; Tian, Q.; Liu, Y.; Ruan, H.; Liu, P.; Wang, Y.; Liu, L. A serial analysis of hydrogen sulfide poisoning: Three group accidents. *Forensic Sci. Med. Pathol.* **2024**, *20*, 1014–1021. [CrossRef] [PubMed]
4. Wu, D.D.; Wang, D.Y.; Li, H.M.; Guo, J.C.; Duan, S.F.; Ji, X.Y. Hydrogen sulfide as a Novel Regulatory Factor in Liver Health and Disease. *Oxidative Med. Cell. Longev.* **2019**, *2019*, 3831713. [CrossRef] [PubMed]
5. Ali, F.I.M.; Awwad, F.; Greish, Y.E.; Mahmoud, S.T. Hydrogen Sulfide (H_2S) Gas Sensor: A Review. *IEEE Sens. J.* **2019**, *19*, 2394–2407. [CrossRef]
6. Liu, H.; Weng, L.; Yang, C. A review on nanomaterial-based electrochemical sensors for H_2O_2, H_2S and NO inside cells or released by cells. *Microchim. Acta* **2017**, *184*, 1267–1283. [CrossRef]
7. Wang, L.; Choi, J. Advances in inorganic conductive material and organic conductive polymer-based resistive gas sensors for room-temperature H_2S detection. *Micro Nano Syst. Lett.* **2025**, *3*, 5. [CrossRef]
8. Korotcenkov, G. Metal oxides for solid-state gas sensors: What determines our choice? *Mater. Sci. Eng. B* **2007**, *139*, 1–23. [CrossRef]
9. Liu, X.; Cheng, S.; Liu, H.; Hu, S.; Zhang, D.; Ning, H. A survey on gas sensing technology. *Sensors* **2012**, *12*, 9635–9665. [CrossRef]
10. Kong, Y.; Li, W.; Zhang, H.; Wang, Z. SnO_2 nanostructured materials used as gas sensors for the detection of hazardous and flammable gases: A review. *Nano Mater. Sci.* **2022**, *4*, 339–350. [CrossRef]
11. Shah, V.; Bhaliya, J.; Patel, G.M.; Joshi, P. Room-temperature chemiresistive gas sensing of SnO_2 nanowires: A review. *J. Inorg. Organomet. Polym. Mater.* **2022**, *32*, 741–772. [CrossRef]
12. Zhao, N.; Chen, Z.; Zeng, W. Enhanced H_2S sensor based on electrospun mesoporous SnO_2 nanotubes. *J. Mater. Sci. Mater. Electron.* **2015**, *26*, 9152–9157. [CrossRef]
13. Berwal, P.; Singh, P.; Sheokand, A.; Rani, S.; Sihag, S.; Bulla, M.; Chaudhary, P.; Gangwar, A.K.; Kumar, V. Fabrication of durable and sensitive SnO_2-Based gas sensor for NO_2 detection. *Appl. Phys. A* **2025**, *131*, 700. [CrossRef]

14. Song, J.; Lin, X.; Ee, L.Y.; Li, S.F.Y.; Huang, M. A Review on Electrospinning as Versatile Supports for Diverse Nanofibers and Their Applications in Environmental Sensing. *Adv. Fiber Mater.* **2023**, *5*, 429–460. [CrossRef]
15. Panigrahi, P.K.; Chandu, B.; Puvvada, N. Recent Advances in Nanostructured Materials for Application as Gas Sensors. *ACS Omega* **2024**, *9*, 3092–3122. [CrossRef] [PubMed]
16. Goswami, Y.C.; Kumar, V.; Rajaram, P.; Malik, M.A.; O'Brien, P. Synthesis of SnO_2 nanostructures by ultrasonic-assisted sol-gel method. *J. Sol-Gel Sci. Technol.* **2014**, *69*, 617–624. [CrossRef]
17. Qian, Y.; Zhang, H.; Xiong, Y.; Wu, Y.; Fu, Z.; Guo, P.; Jiang, H.; Li, J.; Wang, Y.; Yu, S.; et al. Enhanced low-temperature sensitivity of H_2S gas sensing via oxygen vacancy-rich NiO-SnO_2 heterojunction nanostructures. *Microchem. J.* **2025**, *212*, 113177. [CrossRef]
18. Motsoeneng, R.G.; Kortidis, I.; Ray, S.S.; Motaung, D.E. Designing SnO_2 Nanostructure-Based Sensors with Tailored Selectivity toward Propanol and Ethanol Vapors. *ACS Omega* **2019**, *4*, 13696−13709. [CrossRef] [PubMed]
19. Alhadi, A.; Ma, S.; Yang, T.; Pei, S.; Yun, P.; Abbakar, K.A.; Zhang, Q.; Ma, N.; Wang, L.; Balal, M.H.; et al. Pure SnO_2 Gas Sensor with High Sensitivity and Selectivity towards C_2H_5OH. *Adv. Nanopart.* **2021**, *10*, 66–74. [CrossRef]
20. Doubi, Y.; Hartiti, B.; Batan, A.; Siadat, M.; Labrim, H.; Tahiri, M.; Kotbi, A.; Thevenin, P.; Jouiad, M. Controlled SnO_2 nanostructures for enhanced sensing of hydrogen sulfide and nitrogen dioxide. *Sens. Actuators B Chem.* **2025**, *440*, 137878. [CrossRef]
21. Yoon, J.-W.; Choi, S.H.; Kim, J.-S.; Jang, H.W.; Kang, Y.C.; Lee, J.-H. Trimodally porous SnO_2 nanospheres with three-dimensional interconnectivity and size tunability: A one-pot synthetic route and potential application as an extremely sensitive ethanol detector. *NPG Asia Mater.* **2016**, *8*, e244. [CrossRef]
22. Ueda, T.; Torai, S.; Fujita, K.; Shimizu, Y.; Hyodo, T. Effects of Au Addition to Porous CuO2-Added SnO2 Gas Sensors on Their VOC-Sensing Properties. *Chemosensors* **2024**, *12*, 153. [CrossRef]
23. Karmaoui, M.; Jorge, A.B.; McMillan, P.F.; Aliev, A.E.; Pullar, R.C.; Labrincha, J.A.; Tobaldi, D.M. One-Step Synthesis, Structure, and Band Gap Properties of SnO_2 Nanoparticles Made by a Low Temperature Nonaqueous Sol−Gel Technique. *ACS Omega* **2018**, *3*, 13227–13238. [CrossRef] [PubMed]
24. Li, S.-H.; Meng, F.-F.; Chu, Z.; Luo, T.; Peng, F.-M.; Jin, Z. Mesoporous SnO_2 Nanowires: Synthesis and Ethanol Sensing Properties. *Adv. Condens. Matter Phys.* **2017**, *2017*, 9720973. [CrossRef]
25. Gherardi, S.; Astolfi, M.; Gaiardo, A.; Malagù, C.; Rispoli, G.; Vincenzi, D.; Zonta, G. Investigating the Temperature-Dependent Kinetics in Humidity-Resilient Tin–Titanium- Based Metal Oxide Gas Sensors. *Chemosensors* **2024**, *12*, 151. [CrossRef]
26. Wali, Q.; Fakharuddin, A.; Ahmed, I.; Ab Rahim, M.H.; Ismail, J.; Jose, R. Multiporous nanofibers of SnO_2 by electrospinning for high efficiency dye-sensitized solar cells. *J. Mater. Chem. A* **2014**, *2*, 17427. [CrossRef]
27. Ruksana, S.; Kumar, A.; Lakshmy, S.; Kishore, K.R.; Sharma, C.S.; Kumar, M.; Chakraborty, B. Highly Efficient CuO-Anchored SnO_2 Nanofiber for Low-Concentration H_2S Gas Sensors. *ACS Appl. Eng. Mater.* **2024**, *2*, 431–442. [CrossRef]
28. Cai, Z.; Park, S. A superior sensor consisting of porous, Pd nanoparticle–decorated SnO_2 nanotubes for the detection of ppb-level hydrogen gas. *J. Alloys Compd.* **2022**, *907*, 164459. [CrossRef]
29. Su, P.; Li, W.; Zhang, J.; Xie, X. Chemiresistive gas sensor based on electrospun hollow SnO_2 nanotubes for detecting NO at the ppb level. *Vacuum* **2022**, *199*, 110961. [CrossRef]
30. Zhang, J.; Ma, S.; Wang, B.; Pei, S. Preparation of composite SnO_2/CuO nanotubes by electrospinning and excellent gas selectivity to ethanol. *Sens. Actuators A Phys.* **2021**, *332*, 113090. [CrossRef]
31. Bulemo, P.M.; Cho, H.-J.; Kim, N.-H.; Kim, I.-D. Mesoporous SnO_2 Nanotubes via Electrospinning−Etching Route: Highly Sensitive and Selective Detection of H_2S Molecule. *ACS Appl. Mater. Interfaces* **2017**, *9*, 26304–26313. [CrossRef]
32. Kader, M.A.; Azmi, N.S.; Kafi, A.K.M.; Hossain, M.S.; Masri, M.F.B.; Ramli, A.N.M.; Tan, C.S. Synthesis and Characterization of a Multiporous SnO_2 Nanofibers-Supported Au Nanoparticles-Based Amperometric Sensor for the Nonenzymatic Detection of H_2O_2. *Chemosensors* **2023**, *11*, 130. [CrossRef]
33. Güntner, A.T.; Pineau, N.J.; Pratsinis, S.E. Flame-made chemoresistive gas sensors and devices. *Prog. Energy Combust. Sci.* **2022**, *90*, 100992. [CrossRef]
34. Suematsu, K.; Uchiyama, A.; Watanabe, K.; Shimanoe, K. Highly Sensitive Carbon Monoxide Sensor Element with Wide-Range Humidity Resistance by Loading Pd Nanoparticles on SnO_2 Surface. *Sensors* **2022**, *22*, 2934. [CrossRef]
35. Dadkhah, M.; Tulliani, J.-M. Green Synthesis of Metal Oxides Semiconductors for Gas Sensing Applications. *Sensors* **2022**, *22*, 4669. [CrossRef]
36. Zhao, Y.-S.; Huang, J.; Yang, X.; Wang, W.; Yu, D.-G.; He, H.; Liu, P.; Du, K. Electrospun nanofibers and their application as sensors for healthcare. *Front. Bioeng. Biotechnol.* **2025**, *13*, 1533367. [CrossRef]
37. Cho, H.-J.; Kim, Y.H.; Park, S.; Kim, I.-D. Design of Hollow Nanofibrous Structures using Electrospinning: An Aspect of Chemical Sensor Applications. *ChemNanoMat* **2020**, *6*, 1014–1027. [CrossRef]
38. Li, D.; Xia, Y. Electrospinning of Nanofibers: Reinventing the Wheel? *Adv. Mater.* **2004**, *16*, 1151–1170. [CrossRef]
39. Esfahani, H.; Jose, R.; Ramakrishna, S. Electrospun Ceramic Nanofiber Mats Today: Synthesis, Properties, and Applications. *Materials* **2017**, *10*, 1238. [CrossRef] [PubMed]

40. Pascariu, P.; Airineia, A.; Olarua, N.; Petrila, I.; Nica, V.; Sacarescu, L.; Tudorache, F. Microstructure, electrical and humidity sensor properties ofelectrospun NiO–SnO_2 nanofibers. *Sens. Actuators B* **2016**, *222*, 1024–1031. [CrossRef]
41. Reed, J.S. *Principles of Ceramics Processing*; John Wiley & Sons: Hoboken, NJ, USA, 1995.
42. Chen, X.; Hua, Z.; Geng, C.; Ma, N. Facile synthesis of novel $YbFeO_3$–$BiFeO_3$ composite for highly sensitive ppb-level acetone sensing at low temperature. *J. Mater. Sci. Mater. Electron.* **2023**, *34*, 1588. [CrossRef]
43. Busuioc, A.D.; Ciovică, I.; Stoleriu, Ş.; Enculescu, M.; Evanghelidis, A.; Vişan, T. Morphological and optical properties of electrospun SnO_2 fibers. *Dig. J. Nanomater. Biostruct.* **2017**, *12*, 1097–1105.
44. Jang, J.-S.; Kim, S.-J.; Choi, S.-J.; Kim, N.-H.; Hakim, M.; Rothschild, A.; Kim, L.-D. Thin-walled SnO_2 nanotubes functionalized with Pt and Au catalysts via the protein templating route and their selective detection of acetone and hydrogen sulfide molecules. *Nanoscale* **2015**, *7*, 16417–16426. [CrossRef]
45. Wang, L.; Luo, X.; Zheng, X.; Wang, R.; Zhang, T. Direct annealing of electrospun synthesized highperformance porous SnO_2 hollow nanofibers for gas sensors. *RSC Adv.* **2013**, *3*, 9723–9728. [CrossRef]
46. Sing, K.S.W.; Everett, D.H.; Haul, R.A.W.; Moscou, L.; Pierotti, R.A.; Rouquerol, J.; Siemieniewska, T. Reporting physisorption data for gas/solid systems with special reference to the determination of surface area and porosity. *Pure Appl. Chem.* **1985**, *57*, 603–619. [CrossRef]
47. Barsan, N.; Koziej, D.; Weimar, U. Metal oxide-based gas sensor research: How to? *Sens. Actuators B* **2007**, *121*, 18–35. [CrossRef]
48. Wang, C.; Yin, L.; Zhang, L.; Xiang, D.; Gao, R. Metal Oxide Gas Sensors: Sensitivity and Influencing Factors. *Sensors* **2010**, *10*, 2088–2106. [CrossRef] [PubMed]
49. Sun, Y.-F.; Liu, S.-B.; Meng, F.-L.; Liu, J.-Y.; Jin, Z.; Kong, L.-T.; Liu, J.-H. Metal Oxide Nanostructures and Their Gas Sensing Properties: A Review. *Sensors* **2012**, *12*, 2610–2631. [CrossRef] [PubMed]
50. Zhao, J.; Shen, W.; Gao, Y.; Lv, D.; Son, W.; Tan, R. Optimization of SnO_2-based MEMS sensor array for expeditious and precise categorization of meat types and freshness status. *Sens. Actuators A Phys.* **2025**, *391*, 116680. [CrossRef]
51. Lu, Z.; Zhou, Q.; Wang, C.; Wei, Z.; Xu, L.; Gui, Y. Electrospun ZnO–SnO_2 Composite Nanofibers and Enhanced Sensing Properties to SF_6 Decomposition Byproduct H_2S. *Front. Chem.* **2018**, *6*, 540. [CrossRef]
52. Khan, L.A.; Ali, S.; Ali, N.; Zhu, L.; Zulfiqar, S.; Shah, S.; Hussain, S.A.; Shaik, M.R.; Khan, T.; Khan, G.; et al. Investigation of the Fe-doped SnO_2 NPs with enhanced H_2S gas sensing performance. *Ceram. Inter.* **2025**, *51*, 6783–6792. [CrossRef]
53. Mao, L.-W.; Zhu, L.-Y.; Wu, T.T.; Xu, L.; Jin, X.-H.; Lu, H.-L. Excellent long-term stable H_2S gas sensor based on Nb_2O_5/SnO_2 core-shell heterostructure nanorods. *Appl. Surf. Sci.* **2022**, *602*, 154339. [CrossRef]
54. Phuoc, P.H.; Hung, C.M.; Van Toan, N.; Van Duy, N.; Hoa, N.D.; Van Hieu, N. One-step fabrication of SnO_2 porous nanofiber gas sensors for sub-ppm H_2S detection. *Sens. Actuators A Phys.* **2020**, *303*, 111722. [CrossRef]
55. Yang, T.; Boepple, M.; Hémeryck, A.; Jay, A.; Karwounopoulos, S.; Weimar, U.; Barsan, N. H_2S Sensing with SnO_2-Based Gas Sensors: Sulfur Poisoning Mechanism Revealed by Operando DRIFTS and DFT Calculations. *Angew. Chem. Int. Ed.* **2025**, *64*, e202504696. [CrossRef]
56. Lantto, V.; Romppainen, P.; Rantala, T.S.; Leppävuori, S. Equilibrium and Non-equilibrium Conductance Response of Sintered SnO_2 Samples to H_2S. *Sens. Actuators B* **1991**, *4*, 451–455. [CrossRef]

Disclaimer/Publisher's Note: The statements, opinions and data contained in all publications are solely those of the individual author(s) and contributor(s) and not of MDPI and/or the editor(s). MDPI and/or the editor(s) disclaim responsibility for any injury to people or property resulting from any ideas, methods, instructions or products referred to in the content.